analytical chemistry

pubs.acs.org/ac Article

Ultrasensitive Antibiotic Perceiving Based on Aptamer-Functionalized Ultraclean Graphene Field-Effect Transistor Biosensor

Shun Wang, Mingyuan Sun, Yunhong Zhang, Hao Ji, Jianwei Gao, Shuai Song, Jun Sun, Hong Liu, Yu Zhang,* and Lin Han*

Cite This: *Anal. Chem.* 2022, 94, 14785−14793 Read Online

ACCESS | Metrics & More | Article Recommendations | Supporting Information

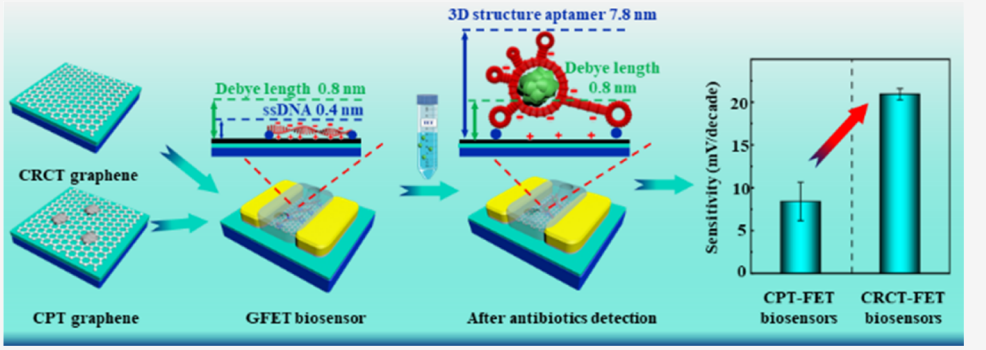

ABSTRACT: Antibiotics are powerful tools to treat bacterial infections, but antibiotic pollution is becoming a severe threat to the effective treatment of human bacterial infections. The detection of antibiotics in water has been a crucial research area for bioassays in recent years. There is still an urgent need for a simple ultrasensitive detection approach to achieve accurate antibiotic detection at low concentrations. Herein, a field-effect transistor (FET)-based biosensor was developed using ultraclean graphene and an aptamer for ultrasensitive tetracycline detection. Using a newly designed camphor−rosin clean transfer (CRCT) scheme to prepare ultraclean graphene, the carrier mobility of the FET is found to be improved by more than 10 times compared with the FET prepared by the conventional PMMA transfer (CPT) method. Based on the FET, aptamer-functionalized transistor antibiotic biosensors were constructed and characterized. A dynamic detection range of 5 orders of magnitude, a sensitivity of 21.7 mV/decade, and a low detection limit of 100 fM are achieved for the CRCT-FET biosensors with good stability, which are much improved compared with the biosensor prepared by the CPT method. The antibiotic sensing and sensing performance enhancement mechanisms for the CRCT-FET biosensor were studied and analyzed based on experimental results and a biosensing model. Finally, the CRCT-FET biosensor was verified by detecting antibiotics in actual samples obtained from the entrances of Bohai Bay.

INTRODUCTION

Antibiotics have made remarkable contributions to medical health and food safety because of their effectiveness in inhibiting the growth of pathogens.[1−4] However, the ensuing problem of antibiotic abuse has caused severe environmental pollution, especially in aquatic environments with excessive antibiotic levels. Antibiotic levels in water are of great concern because they are directly related to people's health, and the accurate detection of antibiotics in the water environment has become a key research area. Tobramycin in the antibiotic family has been successfully detected.[5] The widespread use of tetracycline has elevated its detection needs. The traditional methods used for the detection of antibiotics in water mainly include liquid chromatography−mass spectrometry,[6] liquid chromatography-ultraviolet detection (HPLC/UV),[7] liquid chromatography-fluorescence (HPLC/FD),[8] and Raman spectroscopy.[9] These methods rely on professional equipment and technicians and require complex pretreatment. In recent years, biochemical sensors based on fluorescence,[10] colorimetry,[11] transistors,[12] and electrochemistry[13] have achieved fruitful results for biological detection and have been widely developed for antibiotic detection. Among these approaches, field-effect transistor (FET)-based biosensors provide a reliable, environmentally friendly, sensitive, reliable, simple, and convenient

Received: August 25, 2022
Accepted: October 4, 2022
Published: October 12, 2022

https://doi.org/10.1021/acs.analchem.2c03732
Anal. Chem. 2022, 94, 14785−14793

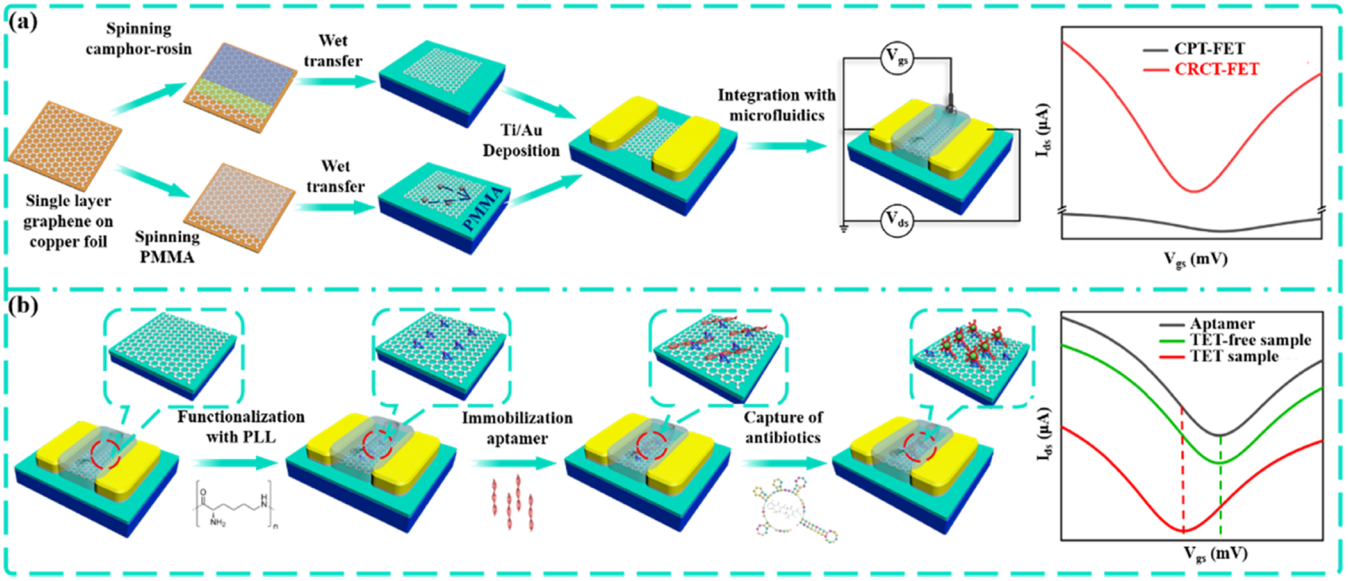

Figure 1. Schematic diagram of (a) graphene field-effect transistor construction and (b) the fabrication process for the biosensor.

detection platform and are expected to become a new sensing platform.[12]

Graphene has been widely used for sensing due to its excellent electrical properties.[14−16] Graphene can be prepared by methods such as direct growth on the target base and transfer to the target substrate. Due to factors such as preparation cost and difficulty, researchers most often use the transfer of copper-based monolayer graphene to the target substrate, but this method is prone to introduce impurities, defects, and other problems during the transfer process that can affect the graphene performance.[17]

There have been many conventional PMMA transfer (CPT)-based graphene studies that have achieved fruitful results.[18,19] However, these devices suffer from issues such as large polymer particle residues and more severe doping,[20] resulting in device performance degradation, which makes it a challenge to develop high-performance biosensors. Through the design of transfer methods assisted by easily removable materials (such as rosin and wax), researchers have obtained high-quality graphene with fewer defects, exhibiting lower resistivity and higher carrier mobility.[21,22] Here, we used a novel camphor−rosin double layer-assisted clean transfer (CRCT) method to obtain high-quality graphene and performance-enhanced field-effect transistors with a more than 6-fold improvement in carrier mobility, which provides a reliable platform for building highly sensitive biosensors.

The core steps in constructing FET biosensors are surface functionalization, probe design, and immobilization.[23] For the study of GFET biosensors, we have reported high-performance biosensors by surface functionalization with PLL and GO for antibody and nucleic acid detection.[18,19] In our previous works, we successfully developed biosensors based on either CPT-based graphene FETs or laser-induced graphene FETs for SARS-CoV-2 protein detection using antibodies and RNA detection using complementary single-stranded DNA probes.[18,19,24] Aptamers are short nucleic acid stretches with a specific three-dimensional structure that can be developed with high affinity and specificity to form complexes through interaction with the desired targets (such as DNA, RNA, proteins, and antibiotics)[25] and are perfect for use as sensing probes. FET biosensors using aptamer modification have made positive progress recently with works on divalent cation,[26] phenylalanine,[27] and avian influenza virus.[28] Aptamer-based GFET biosensors have also been successfully developed for highly sensitive biosensing on geosmin,[29] thrombin,[30] and other substances, providing an empirical basis for aptamer-based sensing. Extensive sensing work has shown that aptamers are excellent sensing probes and exhibit great sensing potential for small molecules such as antibiotics.[31] A rGO-FET biosensor modified by an aptamer was reported for tobramycin detection.[5] A MoS_2 FET with an aptamer probe was also developed for kanamycin detection.[12] Although progress has been made, a high-performance sensing platform still needs to be developed for ultrasensitive antibiotic detection.

Here, a high-performance aptamer-functionalized graphene FET biosensor was used to construct a novel camphor−rosin clean transfer (CRCT) scheme for ultrasensitive antibiotic detection. The performance of the camphor−rosin clean transferred graphene FET (CRCT-FET) and the CRCT-FET antibiotic biosensor were studied and compared with that of conventional PMMA-assisted transferred (CPT) graphene FET (CPT-FET) and CPT-FET biosensors, respectively, which show an improved performance. The enhancement mechanism for the CRCT-FET devices is discussed. Finally, actual sample tests were conducted to analyze the sensing fluctuation factors in complex environments to verify the functional capability and reliability of the CRCT-FET biosensor for applications.

EXPERIMENTAL SECTION

Graphene Transistor and Biosensor Fabrication. The fabrication flows for the FET and biosensor are shown in Figures 1a,b and S1. Detailed information can be found in the Supporting information. As shown in Figure 1a, the CRCT-FET performs much better than the CPT-FET. The V_{Dirac} for the biosensors shifts to the left when antibiotics are present in the solution (red line in Figure 1b). Otherwise, the Dirac point remains in the same position (green line in Figure 1b).

https://doi.org/10.1021/acs.analchem.2c03732
Anal. Chem. 2022, 94, 14785−14793

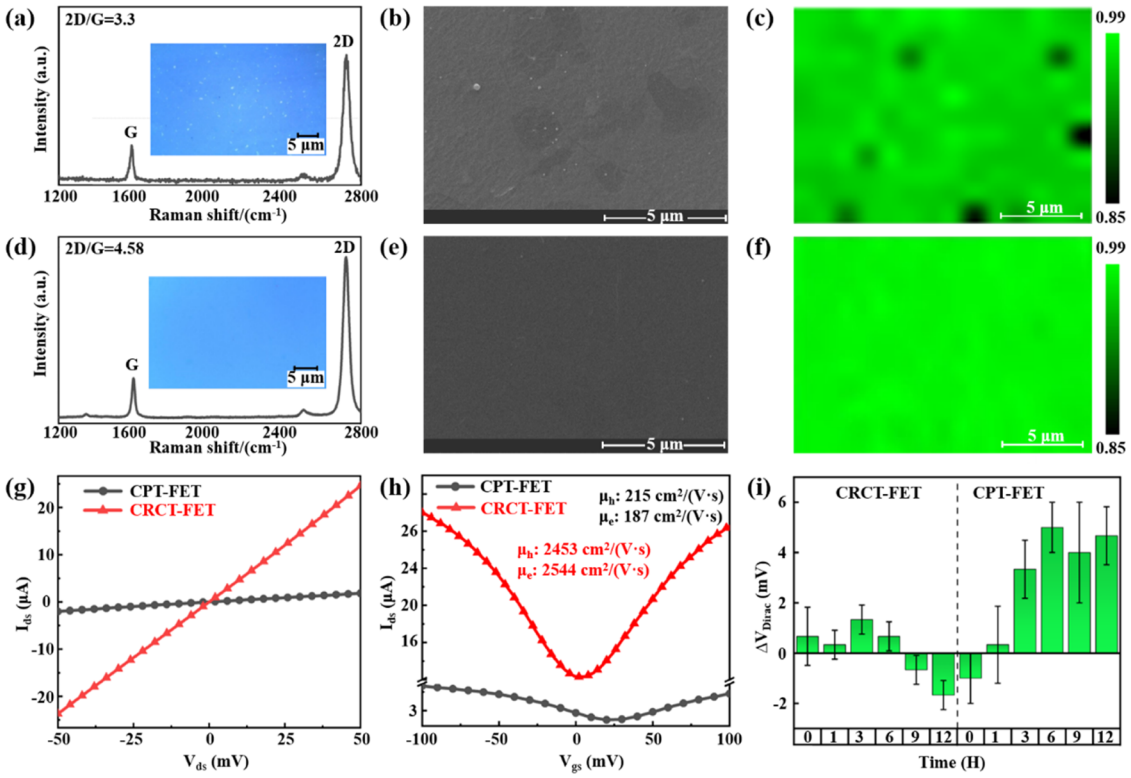

Figure 2. Optical images and Raman spectra for (a) CPT graphene and (d) CRCT graphene; SEM images of (b) CPT graphene and (e) CRCT graphene; Raman mapping images of (c) CPT graphene and (f) CRCT graphene. Output curves (g), transfer curves (h), and stability (i) for the CRCT-FET and CPT-FET (error bars indicate relative standard deviations obtained from three tests).

RESULTS AND DISCUSSION

Characterization of Graphene and GFETs. The optical and SEM images show the PMMA residues on CPT graphene (the bright dots in Figure 2a,b). In contrary, no apparent residues are observed on the CRCT graphene (Figure 2d,e). The AFM image of CRCT graphene (Figure S2a) further confirms the above results, which presents a CRCT graphene RMS surface roughness of 0.51 nm. The Raman spectra (Figure 2a,d) indicate that CRCT graphene exhibits a higher number of monolayers than CPT graphene since the ratio (4.58) of the two-dimensional (2D) peak to the G peak for CRCT graphene is higher than that of 3.3 for CPT graphene.[33] The Raman mapping images also further prove the quality of the CPT and CRCT graphene, as shown in Figure 2c,f, which exhibits the defective Raman mapping image (black dots) for CPT graphene and uniform clear Raman mapping image for CRCT graphene.

To evaluate the electrical characteristics of the constructed GFETs, we measured the output and transfer curves for CRCT-FET and CPT-FET presented in Figure 2g,h. It can be observed that I_{ds} and V_{ds} are linear at constant V_{gs} (Figure 2g), and the conductivity of the CRCT-FET is more than 10 times higher than that of the CPT-FET. The typical bipolar behavior of GFETs is also observed in the transfer curves (Figure 2h).[34] According to the equation for graphene carrier mobility of $\mu = \left(\frac{L}{WCV_{ds}}\right)\left(\frac{dI_{ds}}{dV_{gs}}\right)$,[35] the μ_h and μ_e for the CPT-FET are calculated to be 215 and 187 $cm^2/(V{\cdot}s)$, respectively, and the μ_h and μ_e for the CRCT-FET are calculated to be 2453 and 2544 $cm^2/(V{\cdot}s)$, respectively. The carrier mobility of the CRCT-FET is more than 10 times higher than that of the CPT-FET due to the improvement in the graphene quality obtained through the CRCT process. It has been reported that defects such as polymer residues in CPT graphene result in high contact resistance and low carrier mobility.[36] Meanwhile, the initial V_{Dirac} represents graphene doping. The V_{Dirac} for the CPT-FET offset is obviously to the right of the zero-point due to the p-type doping introduced during the transfer process.[37,38] Surprisingly, the V_{Dirac} for the CRCT-FE is near the zero-point. We infer that this is attributed to the small amount of residue doping through the CRCT process. The stability is another vital evaluation index for FETs, and we present comparative test results for the CPT-FET and CRCT-FET in 12H (Figures 2i and S3). It is observed that the V_{Dirac} for the CRCT-FET is slightly perturbed between −2 and 2 mV, with a standard deviation of 1.08. In comparison, the perturbation range for the CPT-FET ranges between −2 and 6 mV, with a standard deviation of 2.47. The results prove the superior stability of the CRCT-FET. CPT graphene FETs exhibit Dirac point drift due to scattering, poor ohmic contact, and other problems because PMMA residues form during the graphene transfer process, which will become scattering centers, reducing the mean free path in graphene and increasing the contact resistance.[39]

Through the physical characterization and demonstration of the electrical performance, we can conclude that cleaner and less defective high-quality graphene can be prepared by the CRCT process, and high electrical performance graphene field-effect transistors can be constructed based on CRCT graphene, which provides a reliable transistor platform for building highly sensitive biosensors.

Construction and Characterization of the FET Biosensors. First, PLL was functionalized on the channel

https://doi.org/10.1021/acs.analchem.2c03732
Anal. Chem. 2022, 94, 14785−14793

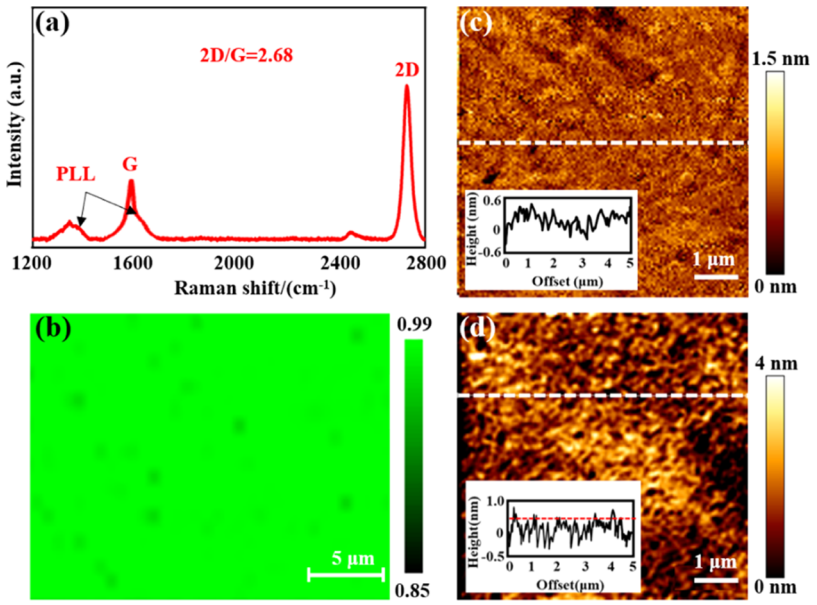

Figure 3. (a) Raman spectrum and (b) Raman mapping of PLL-functionalized graphene. AFM images of (c) PLL/Gr and (d) aptamer/PLL/Gr.

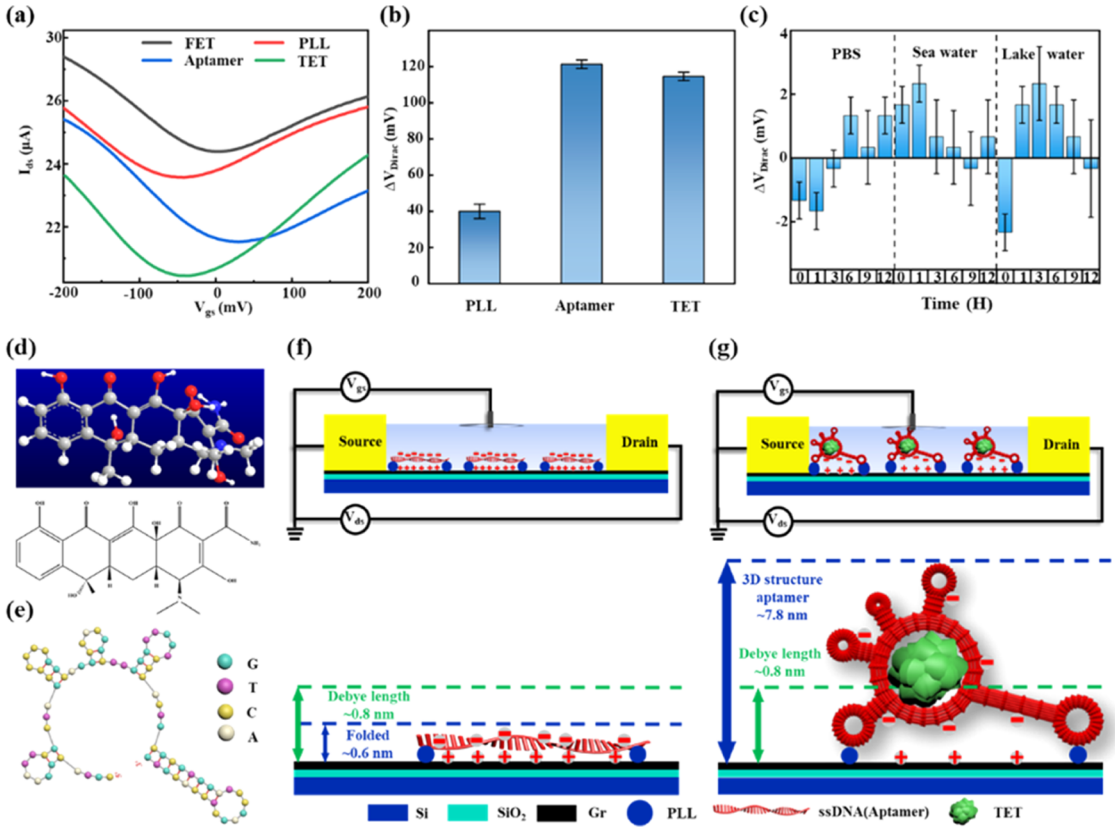

Figure 4. (a) Transfer characteristics and (b) ΔV_{Dirac} for CRCT-FET biosensors; (c) time-dependent ΔV_{Dirac} for CRCT-FET biosensors in different environments; (d) structural schematic of TET; (e) aptamer three-dimensional (3D) structure; (f, g) electrostatic gating mechanism and sensing mechanism for antibiotic detection through the aptamer and TET interaction. In panels (b, c), the error bars indicate relative standard deviations obtained from three tests.

area graphene surface of the GFETs to enhance the sensitivity of the biosensor.[18] Characteristic PLL peaks appear in the Raman spectrum (Figure 3a) after PLL functionalization, which shows the successful surface modification of graphene by PLL.[18] The corresponding mapping image (Figure 3b) shows the uniform PLL surface modification. Then, the aptamer was immobilized on PLL through electrostatic adsorption.[18] The AFM images of PLL/Gr and aptamer/PLL/Gr are presented in Figure 3c,d, respectively. The average height of the surface is increased from ∼0.3 to ∼0.6 nm after aptamer fixation. RMS surface roughness values of 1.14 and 2.38 nm for PLL/Gr and aptamer/PLL/Gr are obtained,

https://doi.org/10.1021/acs.analchem.2c03732
Anal. Chem. 2022, 94, 14785−14793

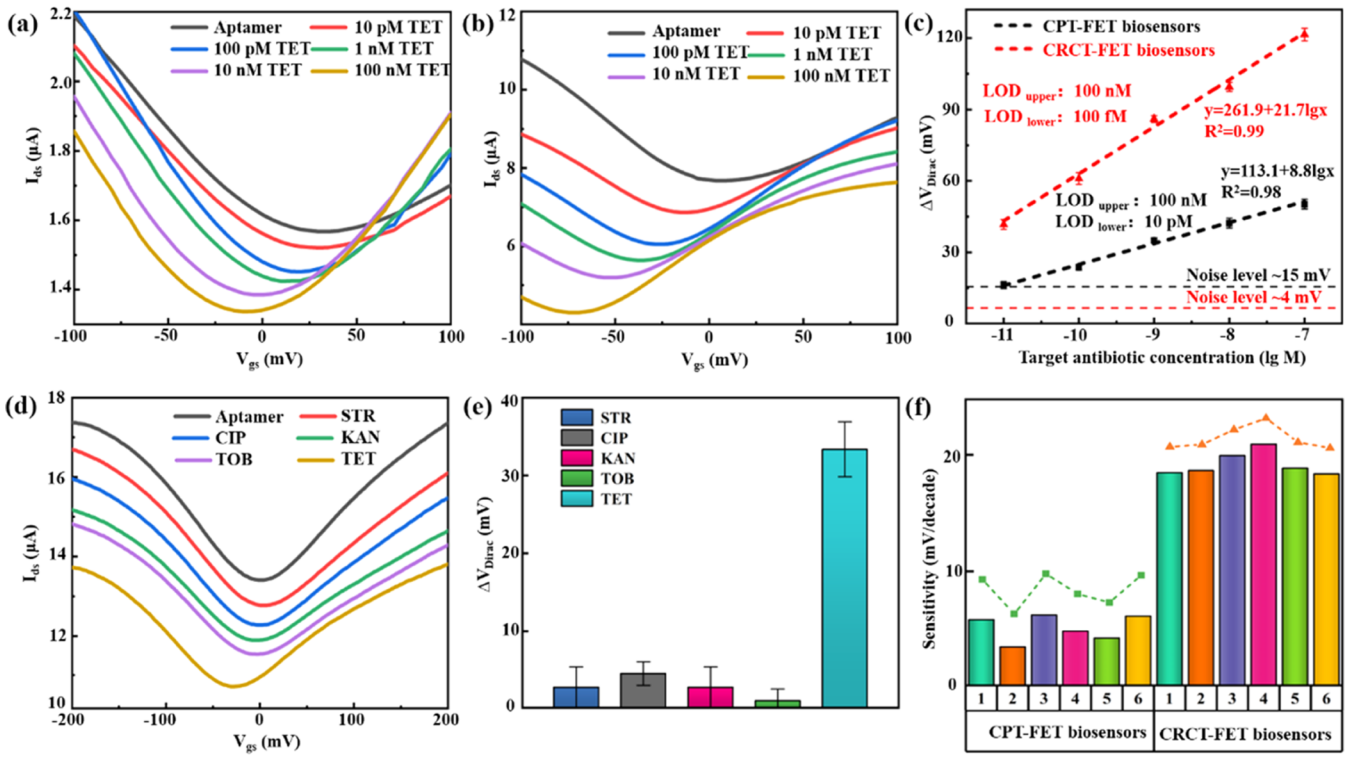

Figure 5. Sensitivity and specificity of CRCT-FET and CPT-FET biosensors. Transfer characteristics of the (a) CPT-FET biosensor and (b) CRCT-FET biosensor at different TET concentrations. (c) TET concentration-dependent ΔV_{Dirac} displacement and fitted linear equations for the CRCT-FET and CPT-FET biosensors. (d–e) Detection results obtained for the CRCT-FET biosensor for 100 pM TET and other antibiotics. (f) Time-dependent stability of the sensitivity of CPT-FET and CRCT-FET biosensors. In panels (c, e), the error bars indicate the relative standard deviations obtained from three tests.

implying successful aptamer immobilization on PLL/Gr. The AFM image of Gr and the changes in the average height after aptamer/PLL modification are presented in Figure S2. These data show an RMS of 0.51 nm and a step height from SiO_2 to the aptamer of ∼2.3 nm, confirming the successful immobilization of Gr and aptamer/PLL on the graphene surface.

To further prove the successful preparation of the biosensors, the electrical characteristics were tested for each build step of the CRCT-FET biosensor, as shown in Figure 4a. The corresponding ΔV_{Dirac} values were calculated, as shown in Figure 4b. Due to the induction of n-doped graphene by the positive charge of PLL, the V_{Dirac} for the CRCT-FET biosensor is left-shifted by approximately 40 mV with PLL modification, which shows the same trend as found in our previous study.[18] The phosphate backbone of the aptamer is negatively charged in solution, and the immobilization of the aptamer on the graphene surface induces graphene p-type doping. The V_{Dirac} for the CRCT-FET biosensor is shifted to the right at ∼121 mV. The V_{Dirac} for the CRCT-FET biosensor is shifted to the left at ∼115 mV due to graphene n-type doping triggered by aptamer deformation after 100 nM target TET incubation hybridization with the aptamer. In contrast, the CPT-FET biosensor exhibits the same trend but with a smaller V_{Dirac} shift value (Figure S4). Electrical tests for the biosensors confirm the successful establishment of the biosensor and that the CRCT method can be used to improve the performance of the biosensor.

To evaluate the stability of the biosensor, we tested the time-dependent electrical properties of CRCT-FET biosensors in PBS, seawater, and lake water. The results are shown in Figures 4c and S5. We can observe that the perturbation range for the CRCT-FET biosensors ranges between −2 and 2 mV, with a standard deviation of 0.95 in PBS, between −2 and 3 mV, with a standard deviation of 1.28 in seawater, and between -3 and 4 mV, with a standard deviation of 1.78 in seawater. The CPT-FET biosensors deliver large perturbation ranges, as shown in Figure S6. The results indicate that the CRCT-FET biosensor shows excellent stability in different environments, which can provide a reliable basis for tetracycline detection.

Principle for the Detection of Antibiotics by the Biosensor. To explore the mechanism for sensing the aptamer in this work, we first tested the nonspecific recognition of TET by bare graphene (Figure S7), where V_{Dirac} is slightly shifted due to the $\pi-\pi$ interaction between graphene and TET. TET molecules are positively charged due to the hydrolysis effect of amino groups ($-NH_2 + H_2O \rightleftharpoons -NH_3^+ + OH^-$), as shown in Figure 4d, which leads to a reduction of the hole density in the graphene surface and a left shift of the V_{Dirac}. After aptamer (Figure 4e) functionalization, the sensing signal strength and stability are both dramatically improved through a change in spatial conformation to achieve specific capture of TET.[32] As reported the aptamer binding to its target is a highly specific interaction.[40] The aptamer can specifically bind to its targets with high affinity.[41] Therefore, there could not be any difference in the binding properties of the original aptamer and the 3D aptamer.

The Debye shielding theory can be used to explain the electrostatic interaction of charged ions in a solution with other ions. The farthest effective distance is defined as the Debye length.[42] According to previous studies,[18,43] the Debye length in 1× PBS is ∼0.8 nm, and PLL surface modification

https://doi.org/10.1021/acs.analchem.2c03732
Anal. Chem. 2022, 94, 14785−14793

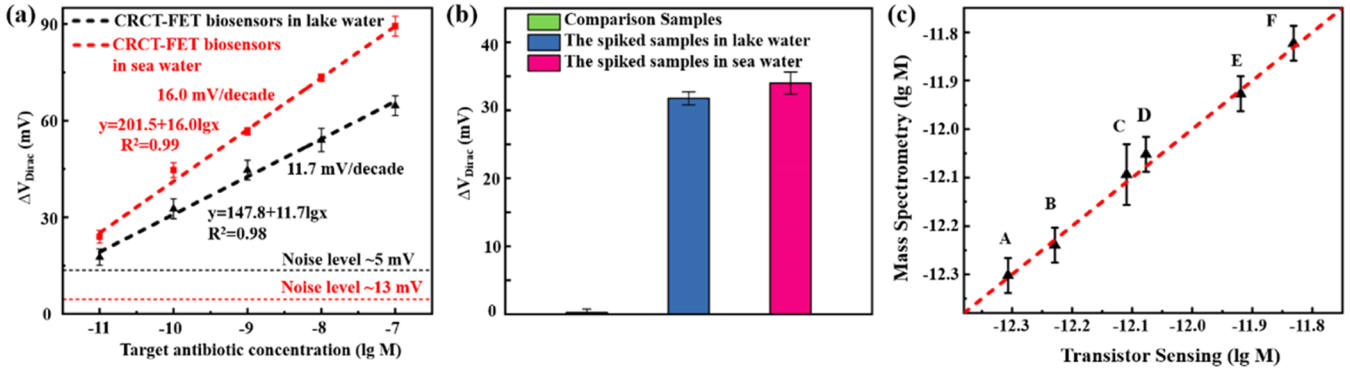

Figure 6. (a) TET concentration-dependent ΔV_{Dirac} displacement and fitted linear equations of the CRCT-FET biosensor for TET detection in seawater and lake water. (b) ΔV_{Dirac} of the CRCT-FET biosensors for the spiked samples in lake water and seawater. (c) Comparison of the TET detection results between the CRCT-FET biosensor and mass spectrometry for the actual samples obtained from the entrances in Bohai Bay. In panels (a–c), the error bars indicate relative standard deviations obtained from three tests.

and aptamer fixation do not affect the Debye length. Figures 4f,g and 3d show that the single-stand aptamer is immobilized on PLL/Gr and lies in the Debye length domain since the single base of the nucleic acid is ~0.6 nm (Figure 4f). After the TET reaction with the aptamer, the aptamer forms the 3D structure aptamer with an overall height of 7.8 nm (Figure 4g). Most of the 3D structure aptamer moves out of the Debye length domain, leading to a reduction in the hole density in the graphene channel, resulting in a change in the graphene doping level. The electrostatic gating mechanism explains the shift in the V_{Dirac}. The reduction in the hole density induces a leftward shift for V_{Dirac} (n-doping).[4] Therefore, the biosensor shows a V_{Dirac} shift. To further verify the sensing principle, we fixed the preannealed aptamer on the channel surface, where the aptamer formed a secondary structure on the CRCT-FET before interaction with the TET. As shown in Figure S8, a weak and unstable sensing signal appears after the TET reaction with the aptamer, which indicates that the TET will not induce a stable sensing signal. The main reason for this is that the interaction position between TET and the 3D-structured aptamer exceeds the Debye length domain (Figures 4g and S9).

To further confirm the sensing mechanism, we replaced the 1× PBS buffer solution with 0.1× PBS, which elevated the Debye length to 8 nm for comparison experiments (Figures S10 and S11). When the Debye length is increased to 8 nm in 0.1× PBS, the sensing signal of the sensor is reduced to 1/5 of that in 1× PBS. It can be predicted that the sensing signal mainly originates from the TET in 0.1× PBS, and the deformation of the aptamer no longer contributes to the sensing signal, resulting in weak sensing signals, which further proves the aptamer-based antibiotic sensing mechanism.

Therefore, it can be concluded that the primary sensing mechanism for TET detection using the aptamer/PL/graphene biosensor is that the change in the aptamer structure induces an electrostatic gating effect due to the TET and aptamer interaction.

Performance of the CRCT-FET and CPT-FET Biosensors. To demonstrate the sensitivity of the biosensors, we tested the antibiotic samples with different concentrations in the range of 10 pM to 100 nM. The results are shown in Figure 5a–c. We can observe that V_{Dirac} gradually shifts to the left with increasing TET concentration (Figure 5a,b). The sensitivity of the CRCT-FET biosensor reaches up to 21.7 mV/decade, with a correlation coefficient R^2 = 0.99 (Figure 5c (red line)). In contrast, the sensitivity of the CPT-FET biosensor is only 8.8 mV/decade, with R^2 = 0.98 (Figure 5c (black line)). The sensitivity of the biosensor through the CRCT method is improved 2.47 times. The detection limits are important sensing metrics, as shown in Figures 5c and S14. The upper detection limit is 100 nM, according to the standard detection limit equation of LOD = $3S_{b1}/S$.[45] The lower detection limit for the CPT-FET biosensor is calculated to be $10^{-11.7}$ M, while the detection limit of the CRCT-FET biosensor reaches $10^{-12.96}$ M.

To verify the specificity of the biosensor, we tested four 100 pM antibiotic samples associated with tetracycline (streptomycin (STR), ciprofloxacin (CIP), kanamycin (KAN), and tobramycin (TOB). The tested results are shown in Figure 5d,e. For nontarget antibiotic samples, the ΔV_{Dirac} values for the CRCT-FET biosensor are all less than 5 mV. For the target antibiotic TET, the ΔV_{Dirac} is greater than 30 mV, which gives a difference of more than 5 times. The results indicate that the CRCT-FET biosensors have a reasonable specificity for the target TET.

We also repeated the experiment several times to evaluate the reproducibility of the biosensors. The sensitivity data for the six groups of CPT-FET and CRCT-FET biosensors are presented in Figures 5f and S12 and S13. The mean sensitivity of the CRCT-FET biosensor is 19.4 mV/decade, with a standard deviation of 1.78 mV/decade, and the mean sensitivity of the CPT-FET biosensor is only 8.5 mV/decade, with a standard deviation of 2.5 mV/decade, which is consistent with the results shown in Figure 5c. All of the results, including the sensitivity, specificity, and reproducibility of the CRCT-FET biosensor, prove that improved sensing performance can be achieved using the CRCT graphene-constructed FET biosensor.

To investigate the reasons behind the improved performance of the CRCT-FET biosensor, we explore the influencing factors for the V_{Dirac} displacement based on EDL theory. The displacement equation for the Dirac point of graphene is given as follows:[44,46,47] $\Delta V_{Dirac} = \frac{e\Delta n}{C_T} \propto \mu, N$, where C_T is the total gate capacitance, Δn is the graphene carrier density variation, μ is the graphene carrier mobility, and N is the number of target molecules on the graphene surface. Therefore, the two parameters of mobility μ and target number N affect the Dirac point shift according to the above equation. As shown in Figure 2, the CRCT-FET has a much higher carrier mobility

https://doi.org/10.1021/acs.analchem.2c03732
Anal. Chem. 2022, 94, 14785−14793

due to the CRCT clean graphene compared to CPT-FET. Therefore, the CRCT-FET biosensors will produce a more significant shift for the same electrical signal, improving the biosensor's sensitivity. In addition, the number of target molecules on the graphene surface is also characterized by the AFM technique.[5] It can be observed that the CRCT-FET biosensors have a higher target molecule density on the graphene surface compared to the CPT-FET biosensors shown in Figure S15 due to the fewer number of defects in the CRCT graphene surface, which will be another important factor for enhancing the sensitivity of the CRCT-FET biosensor. Based on the above analysis, we attribute the improvement in the performance of the CRCT-FET biosensor to the clean graphene obtained by the CRCT process.

Detection of Spiked TET and Actual Samples from the Entrances of Bohai Bay. The detection of actual antibiotic samples has practical applications for environmental protection and water quality inspection. The difficulty in the detection of actual samples compared to standard antibiotic solutions lies in their complex ionic environment. To realize the quantitative detection of actual samples, analyze the influencing factors, and summarize the general methods to enhance the sensing level in a targeted manner, we performed a test of the simulated TET samples in the actual environment. Figures 6a and S16 show the transfer curves obtained for the CRCT-FET biosensors in a seawater environment for different concentrations of antibiotics (TET).

The sensitivity of the CRCT-FET biosensor in seawater is 16.0 mV/decade (R^2 = 0.99) (red line), which decreases to 11.7 mV/decade (R^2 = 0.98) in lake water (black line). To clarify the sensitivity difference in lake water and seawater, the resistivities of the lake water and seawater were measured. The resistivity of the lake water is ∼1097 Ω·cm, which is much higher than the seawater resistivity of 24.56 Ω·cm. The abundant ionic environment in seawater enhances conductivity. At the same time, the enriched ions also produce a perturbation in the sensing signal, which is manifested as an increase in sensitivity.

To simulate the coexistence of multiple antibiotics in the virtual environment, we configured spiked samples in seawater and lake water according to 1 nM equimolar concentrations (TET, KAN, TOB, CIP, and STR) and tested them. Figures 6b and S17 show the signal response of the CRCT-FET biosensor to the spiked samples. Almost no signal response for the comparison samples (KAN, TOB, CIP, and STR) is observed, with a value of 33 mV in seawater and 31 mV in lake water for TET, indicating that the biosensors show an effective signal response in a complex ionic environment.

To further evaluate the practical application of the proposed biosensor, actual samples collected from the entrances of Bohai Bay were tested and compared with the results obtained by mass spectrometry. The actual samples from six locations in Bohai Bay and the results obtained are presented in Table S1. The transmission curves for the CRCT-FET biosensor with actual sample detection are presented in Figure S18. The tested concentrations for the actual samples can be calculated using the sensitivity equation for the CRCT-FET biosensor, as shown in Figure 6a ($y = 147.8 + 11.7\lg x$). A comparison of the results is presented in Figure 6c. The recovery rates range between 98 and 106%, which confirms the reliability of the CRCT-FET biosensor working in real environments.

CONCLUSIONS

In summary, a GFET-based biosensor using CRCT ultraclean graphene and an aptamer was developed for the ultrasensitive detection of tetracycline. Using a newly designed CRCT scheme to prepare ultraclean graphene, the carrier mobility of the GFET is improved by more than 10 times compared with the FET prepared by the CPT method. Based on the FET, aptamer-functionalized transistor antibiotic biosensors were constructed and characterized. A sensing principle for the aptamer-functionalized antibiotic biosensor is proposed, which is based on the electrostatic gating effect induced by aptamer reconstruction after antibiotic and aptamer interactions on the FET channel surface. A dynamic detection range of 5 orders of magnitude, a sensitivity of 21.7 mV/decade, and a low detection limit of 100 fM are achieved with good stability for the CRCT-FET, which is much improved compared with the biosensor prepared by the CPT method. The sensing performance enhancement mechanism for the CRCT-FET biosensor is mainly attributed to the CRCT clean graphene. The CRCT-FET biosensor operation is verified by detecting antibiotics in actual samples from the entrances of Bohai Bay. A recovery rate ranging between 98 and 106% is achieved compared with the results obtained by mass spectrometry, which proves the practical application of the developed biosensor.

ASSOCIATED CONTENT

Supporting Information

The Supporting Information is available free of charge at https://pubs.acs.org/doi/10.1021/acs.analchem.2c03732.

Graphene wet transfer process; detailed experiments; AFM images of Gr and Gr/PLL/Apt/TET; time stability of CPT-FET and CRCT-FET; transfer characteristics for typical CRCT-FET and CPT-FET biosensors; time stability of CPT-FET and CRCT-FET biosensors in different liquid phase environments; transfer characteristics of bare graphene biosensors; reliability experiment to verify the sensing mechanism under 0.1× PBS and pre-annealing conditions; properties of CPT-FET and CRCT-FET biosensors in different fabrication batches; operating linear zone of CRCT-FET biosensors; AFM images proving the signal enhancement mechanism; transfer characteristics of CRCT-FET biosensors in different liquid phase environments; transfer characteristics of CRCT-FET biosensor with spiked samples and actual samples from Bohai Bay; and detection information of actual samples (PDF)

AUTHOR INFORMATION

Corresponding Authors

Yu Zhang − *Institute of Marine Science and Technology, Shandong University, Qingdao 266237 Shandong, China; Shenzhen Research Institute of Shandong University, Shenzhen 518057, China; State Key Laboratory of Microbial Technolgoy, Shandong University, Qingdao 266237, China;* orcid.org/0000-0002-0666-2537; Email: yuzhang@sdu.edu.cn

Lin Han − *Institute of Marine Science and Technology, Shandong University, Qingdao 266237 Shandong, China; Shenzhen Research Institute of Shandong University, Shenzhen 518057, China; State Key Laboratory of Microbial Technolgoy, Shandong University, Qingdao 266237, China;*

https://doi.org/10.1021/acs.analchem.2c03732
Anal. Chem. 2022, 94, 14785−14793

orcid.org/0000-0003-0461-2031; Email: hanlin@sdu.edu.cn

Authors

Shun Wang − *Institute of Marine Science and Technology, Shandong University, Qingdao 266237 Shandong, China*

Mingyuan Sun − *Institute of Marine Science and Technology, Shandong University, Qingdao 266237 Shandong, China*

Yunhong Zhang − *Institute of Marine Science and Technology, Shandong University, Qingdao 266237 Shandong, China*

Hao Ji − *Institute of Marine Science and Technology, Shandong University, Qingdao 266237 Shandong, China*

Jianwei Gao − *Institute of Marine Science and Technology, Shandong University, Qingdao 266237 Shandong, China*

Shuai Song − *Research Center for Eco-Environmental Sciences, Chinese Academy of Sciences, University of Chinese Academy of Sciences, Beijing 100049, China*

Jun Sun − *College of Marine Science and Technology, China University of Geosciences (Wuhan), Wuhan 430074, China;* orcid.org/0000-0001-7369-7871

Hong Liu − *State Key Laboratory of Crystal Materials, Shandong University, Jinan 250100 Shandong, China;* orcid.org/0000-0003-1640-9620

Complete contact information is available at: https://pubs.acs.org/10.1021/acs.analchem.2c03732

Author Contributions

Y.Z. and L.H. designed the research, revised the manuscript, and provided funds; S.W. conducted the experiment and wrote the manuscript draft; M.S., Y.Z., H.J. and J.G. assisted in the test and completed the experiment; H.L. gave theoretical guidance. S.S. and J.S. assisted with actual sample collection from the entrances of Bohai Bay and mass spectrometry method testing.

Notes

The authors declare no competing financial interest.

■ ACKNOWLEDGMENTS

This work was supported by the National Natural Science Foundation of China (No. 62174101), the Major Scientific and Technological Innovation Project of Shandong Province (2021CXGC010603), the Fundamental Research Funds of Shandong University (2020QNQT001), the Key Fundamental Research Program of Shenzhen (JCYJ20210324115601004), State Key Laboratory of Microbial Technology Open Projects Fund (Project Nos. M2021-01 and M2021-07), Collaborative Innovation Center of Technology and Equipment for Biological Diagnosis and Therapy in Universities of Shandong, and Collaborative Innovation Center of Technology and Equipment for Biological Diagnosis and Therapy in Universities of Shandong. The authors would like to thank Haiyan Yu, Xiaomin Zhao, Sen Wang, and Yuyu Guo from the State Key Laboratory of Microbial Technology of Shandong University for their help and guidance in material characterization.

■ REFERENCES

(1) Chen, J.; Ying, G. G.; Deng, W. J. *J. Agric. Food Chem.* **2019**, *67*, 7569−7586.
(2) D'Costa, V. M.; King, C. E.; Kalan, L.; Morar, M.; Sung, W. W.; Schwarz, C.; Froese, D.; Zazula, G.; Calmels, F.; Debruyne, R.; Golding, G. B.; Poinar, H. N.; Wright, G. D. *Nature* **2011**, *477*, 457−461.
(3) Heß, S.; Kneis, D.; Osterlund, T.; Li, B.; Kristiansson, E.; Berendonk, T. U. *Environ. Sci. Technol.* **2019**, *53*, 13898−13905.
(4) Sun, Y.; Zhao, J.; Liang, L. *Microchim. Acta* **2021**, *188*, No. 21.
(5) Chen, X.; Liu, Y.; Fang, X.; Li, Z.; Pu, H.; Chang, J.; Chen, J.; Mao, S. *Biosens. Bioelectron.* **2019**, *126*, 664−671.
(6) Jank, L.; Martins, M. T.; Arsand, J. B.; Motta, T. M. C.; Feijó, T. C.; dos Santos Castilhos, T.; Hoff, R. B.; Barreto, F.; Pizzolato, T. M. *Food Anal. Methods* **2017**, *10*, 2152−2164.
(7) Legrand, T.; Vodovar, D.; Tournier, N.; Khoudour, N.; Hulin, A. *Agents Chemother.* **2016**, *60*, 4734−4742.
(8) Peres, G. T.; Rath, S.; Reyes, F. G. R. *Food Control* **2010**, *21*, 620−625.
(9) Yang, K.; Li, H. Z.; Zhu, X.; Su, J. Q.; Ren, B.; Zhu, Y. G.; Cui, L. *Anal. Chem.* **2019**, *91*, 6296−6303.
(10) Li, B.; Zhou, X.; Liu, H.; Deng, H.; Huang, R.; Xing, D. *ACS Appl. Mater. Interfaces* **2018**, *10*, 4494−4501.
(11) Chen, F. E.; Kaushik, A.; Hsieh, K.; Chang, E.; Chen, L.; Zhang, P.; Wang, T. H. *Anal. Chem.* **2021**, *93*, 1260−1265.
(12) Chen, X.; Hao, S.; Zong, B.; Liu, C.; Mao, S. *Biosens. Bioelectron.* **2019**, *145*, No. 111711.
(13) Kling, A.; Chatelle, C.; Armbrecht, L.; Qelibari, E.; Kieninger, J.; Dincer, C.; Weber, W.; Urban, G. *Anal. Chem.* **2016**, *88*, 10036−10043.
(14) Park, I.; Lim, J.; You, S.; Hwang, M. T.; Kwon, J.; Koprowski, K.; Kim, S.; Heredia, J.; Stewart de Ramirez, S. A.; Valera, E.; Bashir, R. *ACS Sens.* **2021**, *6*, 4461−4470.
(15) Yu, Y.; Li, Y. T.; Jin, D.; Yang, F.; Wu, D.; Xiao, M. M.; Zhang, H.; Zhang, Z. Y.; Zhang, G. J. *Anal. Chem.* **2019**, *91*, 10679−10686.
(16) Danielson, E.; Sontakke, V. A.; Porkovich, A. J.; Wang, Z.; Kumar, P.; Ziadi, Z.; Yokobayashi, Y.; Sowwan, M. *Sens. Actuators, B* **2020**, *320*, No. 128432.
(17) Kim, S.; Shin, S.; Kim, T.; Du, H.; Song, M.; Lee, C.; Kim, K.; Cho, S.; Seo, D. H.; Seo, S. *Carbon* **2016**, *98*, 352−357.
(18) Gao, J.; Wang, C.; Wang, C.; Chu, Y.; Wang, S.; Sun, M. Y.; Ji, H.; Gao, Y.; Wang, Y.; Han, Y.; Song, F.; Liu, H.; Zhang, Y.; Han, L. *Anal. Chem.* **2022**, *94*, 1626−1636.
(19) Gao, J.; Wang, C.; Chu, Y.; Han, Y.; Gao, Y.; Wang, Y.; Wang, C.; Liu, H.; Han, L.; Zhang, Y. *Talanta* **2022**, *240*, No. 123197.
(20) Yang, X.; Yan, M. *Nano Res.* **2020**, *13*, 599−610.
(21) Zhang, Z.; Du, J.; Zhang, D.; Sun, H.; Yin, L.; Ma, L.; Chen, J.; Ma, D.; Cheng, H. M.; Ren, W. *Nat. Commun.* **2017**, *8*, No. 14560.
(22) Qi, P.; Huang, Y.; Yao, Y.; Li, Q.; Lian, Y.; Lin, L.; Wang, X.; Gu, Y.; Li, L.; Deng, Z.; Peng, Y.; Liu, Z. *Appl. Surf. Sci.* **2019**, *493*, 81−86.
(23) Vu, C. A.; Chen, W. Y. *Sensors* **2019**, *19*, No. 4214.
(24) Cui, T. R.; Qiao, Y. C.; Gao, J. W.; Wang, C. H.; Zhang, Y.; Han, L.; Yang, Y.; Ren, T. L. *Molecules* **2021**, *26*, No. 6947.
(25) Zhou, W.; Huang, P. J.; Ding, J.; Liu, J. *Analyst* **2014**, *139*, 2627−2640.
(26) Nakatsuka, N.; Abendroth, J. M.; Yang, K. A.; Andrews, A. M. *ACS Appl. Mater. Interfaces* **2021**, *13*, 9425−9435.
(27) Cheung, K. M.; Yang, K. A.; Nakatsuka, N.; Zhao, C.; Ye, M.; Jung, M. E.; Yang, H.; Weiss, P. S.; Stojanovic, M. N.; Andrews, A. M. *ACS Sens.* **2019**, *4*, 3308−3317.
(28) Kwon, J.; Lee, Y.; Lee, T.; Ahn, J. H. *Anal. Chem.* **2020**, *92*, 5524−5531.
(29) Park, S. J.; Seo, S. E.; Kim, K. H.; Lee, S. H.; Kim, J.; Ha, S.; Song, H. S.; Lee, S. H.; Kwon, O. S. *Biosens. Bioelectron.* **2021**, *174*, No. 112804.
(30) Yu, H.; Zhao, Z.; Xiao, B.; Deng, M.; Wang, Z.; Li, Z.; Zhang, H.; Zhang, L.; Qian, J.; Li, J. *Anal. Chem.* **2021**, *93*, 13673−13679.
(31) Mehlhorn, A.; Rahimi, P.; Joseph, Y. *Biosensors* **2018**, *8*, 54.
(32) Niazi, J. H.; Lee, S. J.; Gu, M. B. *Bioorg. Med. Chem.* **2008**, *16*, 7245−7253.
(33) Ferrari, A. C.; Basko, D. M. *Nat. Nanotechnol.* **2013**, *8*, 235−246.
(34) Sun, M.; Zhang, C.; Wang, J.; Sun, C.; Ji, Y.; Cheng, S.; Liu, H. *Adv. Electron. Mater.* **2020**, *6*, No. 2000731.

(35) Wu, G.; Dai, Z.; Tang, X.; Lin, Z.; Lo, P. K.; Meyyappan, M.; Lai, K. W. C. *Adv. Healthcare Mater.* **2017**, *6*, No. 2000731.
(36) Giubileo, F.; Di Bartolomeo, A. *Prog. Surf. Sci.* **2017**, *92*, 143−175.
(37) Zhuang, B.; Li, S.; Li, S.; Yin, J. *Carbon* **2021**, *173*, 609−636.
(38) Leong, W. S.; Wang, H.; Yeo, J.; Martin-Martinez, F. J.; Zubair, A.; Shen, P. C.; Mao, Y.; Palacios, T.; Buehler, M. J.; Hong, J. Y.; Kong, J. *Nat. Commun.* **2019**, *10*, No. 867.
(39) Gao, Y.; Chen, J.; Chen, G.; Fan, C.; Liu, X. *Small Methods* **2021**, *5*, No. 2100771.
(40) Lorenz, C.; Schroeder, R.*In The Aptamer Handbook*; Wiley: 2006; pp 116−130.
(41) Pan, H.; Dong, Y.; Gong, L.; Zhai, J.; Song, C.; Ge, Z.; Su, Y.; Zhu, D.; Chao, J.; Su, S.; Wang, L.; Wan, Y.; Fan, C. *Biosens. Bioelectron.* **2022**, *215*, No. 114553.
(42) Bhattacharyya, I. M.; Shalev, G. *ACS Sens.* **2020**, *5*, 154−161.
(43) Hwang, M. T.; Heiranian, M.; Kim, Y.; You, S.; Leem, J.; Taqieddin, A.; Faramarzi, V.; Jing, Y.; Park, I.; van der Zande, A. M.; Nam, S.; Aluru, N. R.; Bashir, R. *Nat. Commun.* **2020**, *11*, No. 1543.
(44) Fu, W.; Jiang, L.; van Geest, E. P.; Lima, L. M.; Schneider, G. F. *Adv. Mater.* **2017**, *29*, No. 1603610.
(45) Chu, Y.; Gao, Y.; Tang, W.; Qiang, L.; Han, Y.; Gao, J.; Zhang, Y.; Liu, H.; Han, L. *Anal. Chem.* **2021**, *93*, 5129−5136.
(46) Uesugi, E.; Goto, H.; Eguchi, R.; Fujiwara, A.; Kubozono, Y. *Sci. Rep.* **2013**, *3*, No. 1595.
(47) Dontschuk, N.; Stacey, A.; Tadich, A.; Rietwyk, K. J.; Schenk, A.; Edmonds, M. T.; Shimoni, O.; Pakes, C. I.; Prawer, S.; Cervenka, J. *Nat. Commun.* **2015**, *6*, No. 6563.

https://doi.org/10.1021/acs.analchem.2c03732
Anal. Chem. 2022, 94, 14785−14793